

Electronic Supplementary Information (ESI) for

3D printing-directed auxetic Kevlar aerogel architectures with multi-functionalizable properties

*Qingqing Cheng,^{a,b} Yang Liu,^c Jing Lyu,^b Qiang Lu,^d Xuotong Zhang ^{*b,e} and Wenhui Song ^{*e}*

^aSchool of Nano-Tech and Nano-Bionics, University of Science and Technology of China, Hefei 230026, P. R. China.

^bSuzhou Institute of Nano-Tech and Nano-Bionics, Chinese Academy of Sciences, Suzhou 215123, P. R. China.

^cDepartment of Materials, Imperial College London SW7 2AZ, UK.

^dNational Engineering Laboratory for Modern Silk, Soochow University, Suzhou 215123, P.R. China.

^eCentre for Biomaterials in Surgical Reconstruction and Regeneration, Division of Surgery and Interventional Science, University College London, London NW3 2PF, UK.

*E-mail: xtzhang2013@sinano.ac.cn (X. Zhang), w.song@ucl.ac.uk (W. Song)

Figures of the Supporting Information

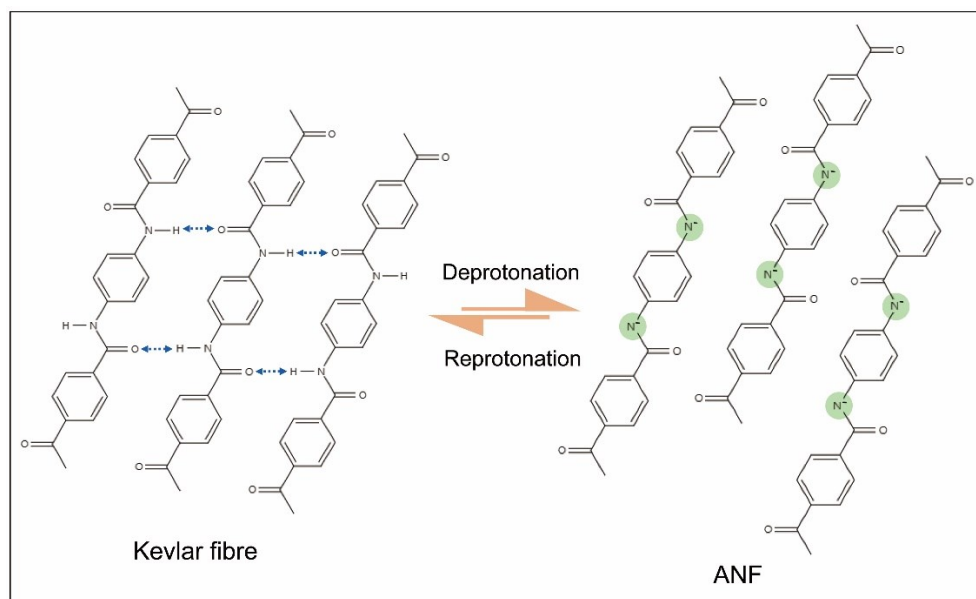


Fig. S1 The chemistry of Kevlar fibre and ANF during the deprotonation and reprotonation process. The macroscopic Kevlar fibre was deprotonated in a KOH/DMSO system by abstracting the mobile hydrogen from amide group and generated negatively charged polyanions subsequently. With the negative charges gradually gathered on the polymer chains during the continuous deprotonation process, the increasing electrostatic repulsion drastically reduced the strength of hydrogen bonds between the polymer chains, which finally resulted in the formation of the high-aspect-ratio ANF.^{1,2} Finally, a homogeneous ANF/DMSO dispersion was achieved. The subsequent solvent exchange between as-printed 3D ANF cryogel with water (employed as a proton donor to reprotonate the polyanions) was expected to regenerate more additional hydrogen bonds between water and NH functional groups on ANFs due to the energetically favourable N-H...O=C interaction in water.³

Ultimately, the 3D Kevlar hydrogel architecture consisting of entangled nanofibres were formed.

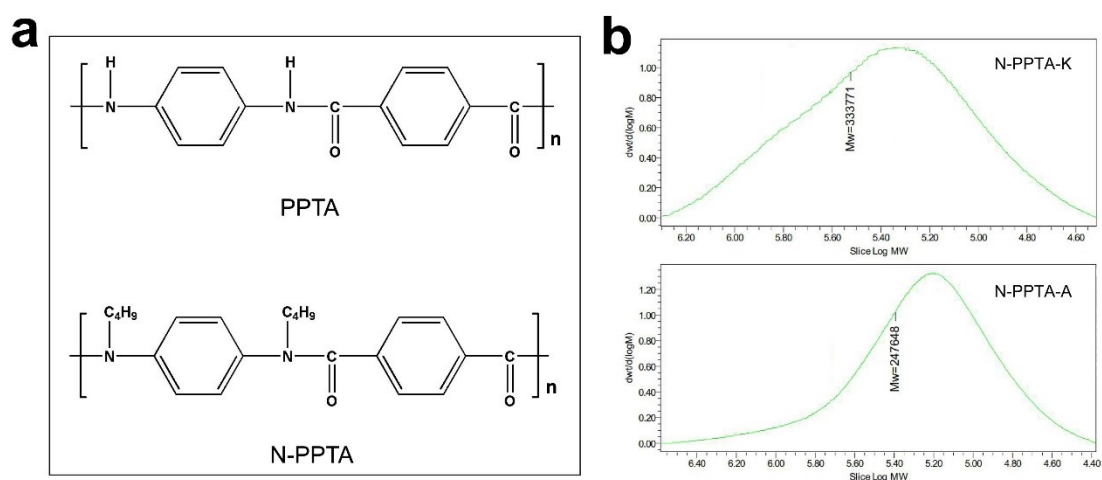


Fig. S2 (a) The chemical structures of PPTA and N-butylated PPTA. (b) GPC curves of N-PPTA-K and N-PPTA-A. Because of the energetic hydrophobic attraction and π - π stacking in the polymer backbone, the extent of deprotonation of Kevlar fibre resulted from KOH/DMSO system is limited and does not appear to proceed down to the level of individual polymer chain.³ The ANF existing in the form of nanofibre in KOH/DMSO system consists of lots of polymer chains. In order to obtain the molecular weight (M_w) and polydispersity index (PDI) of Kevlar fibre and ANF, modification of the Kevlar fibre and ANF by alkylation were carried according to the literatures.^{4,5} The method is as follows. 0.15 g sodium hydride (60% dispersion in mineral oil) was dissolved in the 25 ml anhydrous DMSO under a nitrogen atmosphere, and then 0.25 g dried Kevlar fibre or ANF was dissolved completely into the above-mentioned clear solution respectively. The N-PPTA-K (N-butylated PPTA prepared based Kevlar fibre) and N-PPTA-A (N-butylated PPTA prepared based ANF) were obtained after 250 μ L n-Butyl bromide was added and stirred for 20 h.

The N-PPTA-K and N-PPTA-A were precipitated in deionized water followed by washing with deionized water and acetone. For the gel permeation chromatography (GPC), the dried N-PPTA-K and N-PPTA-A were dissolved into dimethyl formamide (DMF) at a concentration of 0.5 mg ml⁻¹. The GPC results demonstrated that the M_w and PDI of N-PPTA-K is 333,771 and 1.82 while M_w and PDI of N-PPTA-A is 247,648 and 1.84 respectively. Assumption that the degree of substitution is 100 %, the M_w and PDI of PPTA-K is 225,674 and 1.82 while M_w and PDI of PPTA-A is 167,443 and 1.84 respectively in according to the following formula:

$$M_w(N-PPTA) = M_a \times M_w(PPTA) / M_b \quad (1)$$

Where M_a and M_b are the molecular weight of the repeating unit of the N-PPTA and PPTA. The values are 352 and 238 respectively. These results indicate that KOH will degrade the polymeric chain of the Kevlar and increase the MD slightly during dispersing of Kevlar in DMSO.

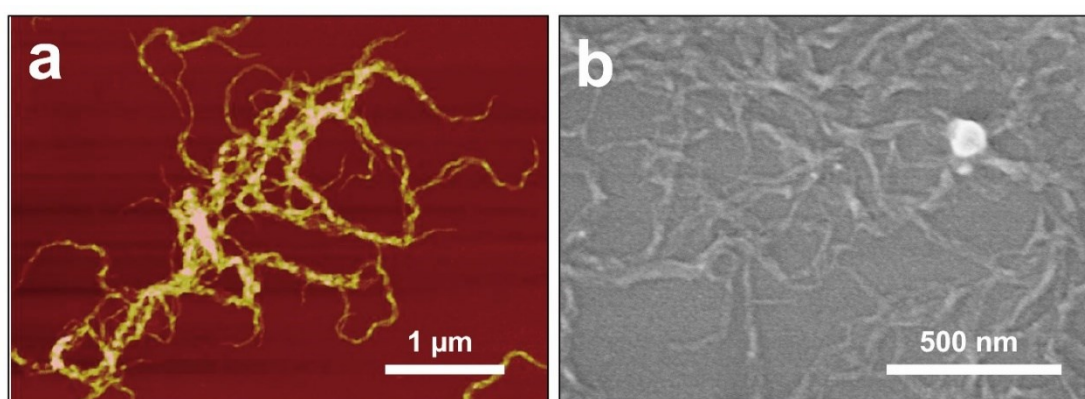


Fig. S3 AFM (a) and SEM (b) images of the morphology of ANF. The high-aspect-ratio ANFs with 5–30 nm in diameter and several micrometers in length, which demonstrated that the Kevlar fibre was spilt into nanofibres successfully.

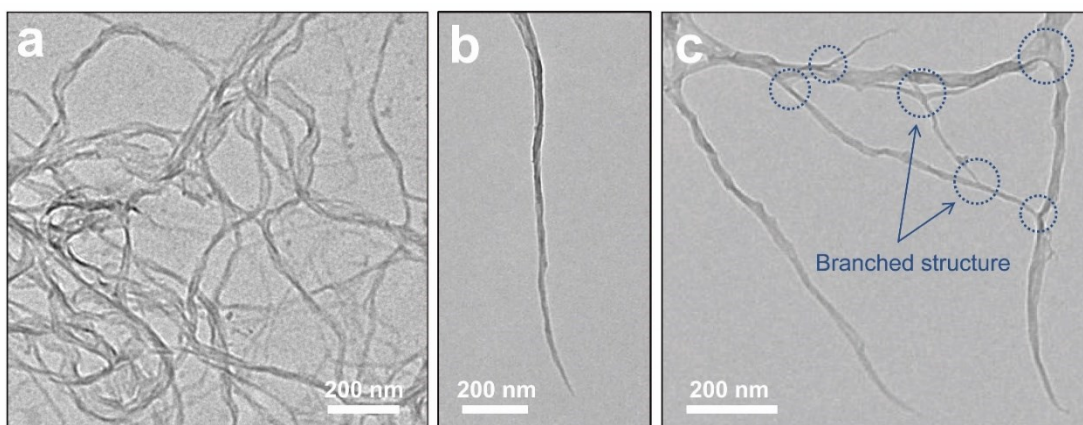


Fig. S4 TEM images of the morphology of entangled ANF showing the branched structure, which is similar to the literature.⁶

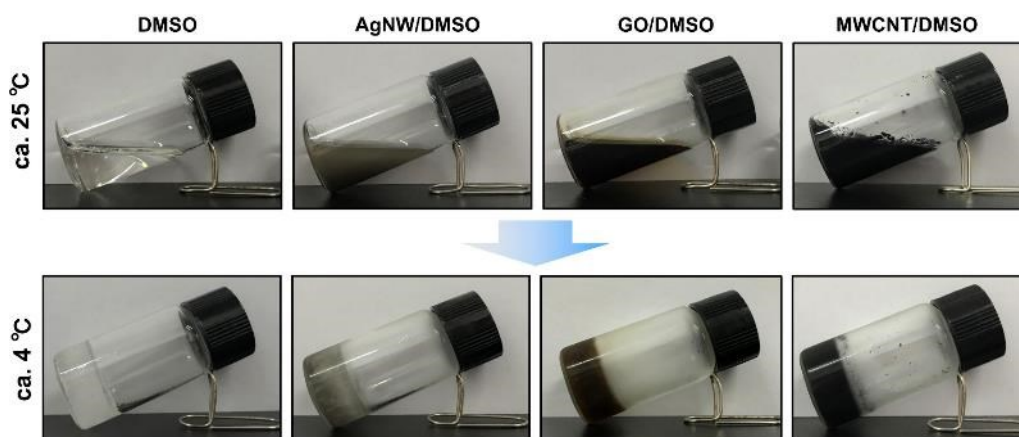


Fig. S5 Digital photos of DMSO, AgNW/DMSO, GO/DMSO and MWCNT/DMSO dispersions at *ca.* 25 °C and *ca.* 4 °C, respectively. These four dispersions are all liquid state at *ca.* 25 °C but frozen state at *ca.* 4 °C due to the high freezing point of DMSO, demonstrating a favorable condition for DIW under low-temperature.

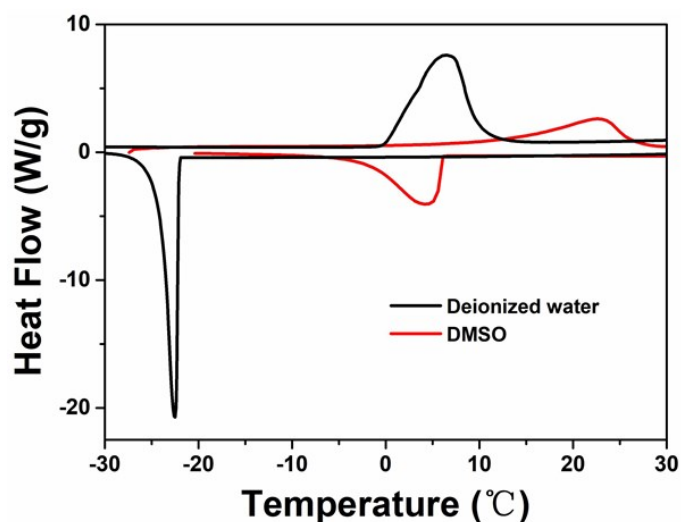


Fig. S6 The DSC curves of the deionized water and DMSO at a scan rate of $10\text{ }^{\circ}\text{C}\cdot\text{min}^{-1}$. Because of the supercooling phenomenon, the crystallization temperature (T_c) of the deionized water is $-22.5\text{ }^{\circ}\text{C}$, much lower than the T_c of DMSO ($-0.08\text{ }^{\circ}\text{C}$), demonstrating that the DMSO-based inks are favorable for DIW under low-temperature.

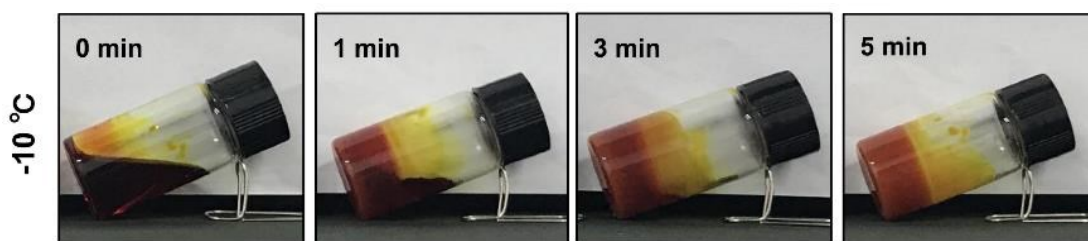


Fig. S7 The digital photos of ANF/DMSO dispersion standing still at $-10\text{ }^{\circ}\text{C}$ for different time. The DMSO/ANF dispersions crystallized gradually with an increase of crystallization time under $-10\text{ }^{\circ}\text{C}$.

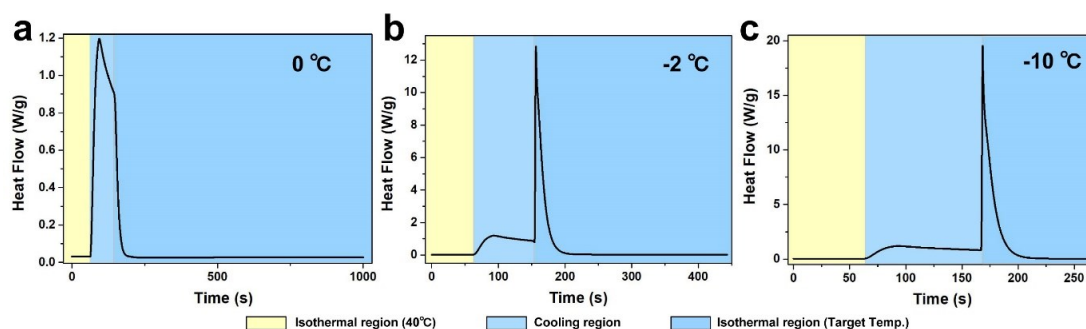


Fig. S8 The original isothermal crystallisation curves of heat flow as a function of time by quenching the ink from molten state (40 °C) to different crystallization temperatures (0, -2, -10 °C) at a cooling rate of 200 °C·min⁻¹ respectively, from which the Fig. 1d was calculated.

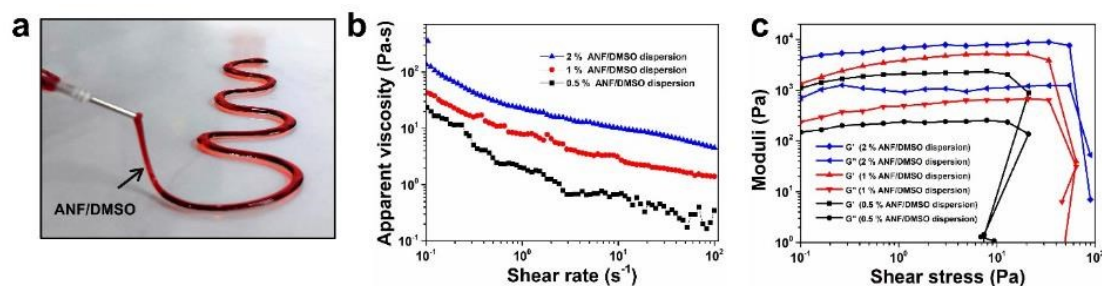


Fig. S9 Rheological properties of the ANF/DMSO dispersion: (a) the digital photo of the ANF/DMSO dispersion extruded by a syringe needle. (b-c) Log-log plots of apparent viscosity as a function of shear rate (b) and dynamic stress sweep from 10⁻¹ to 10² Pa at a constant frequency of 1 Hz showing the storage and loss modulus as a function of shear stress (c) of 0.5 wt%, 1 wt% and 2 wt% ANFs. The obvious shear thinning behavior and highest viscosity as well as modulus are observed from 2 wt% ANF/DMSO dispersions which are favorable for DIW.

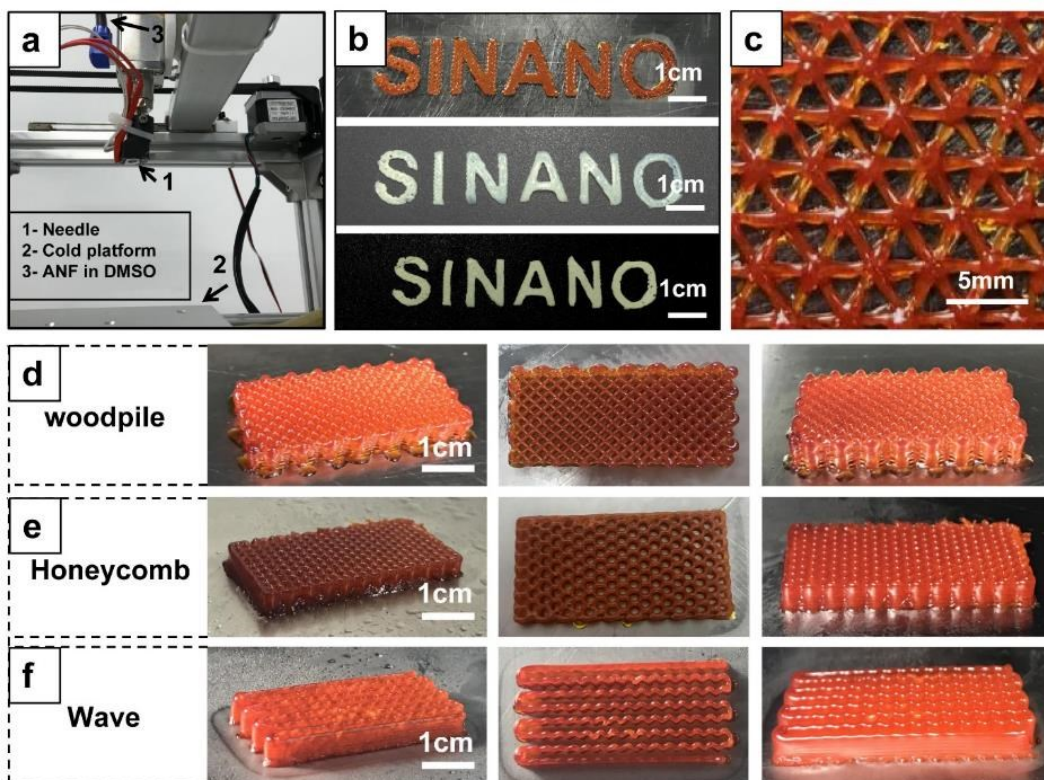


Fig. S10 3D printing Kevlar nanofibre gel process. (a) The 3D printing setup. (b) The 3D printed letters of Kevlar cryogels (top), corresponding hydrogels after solvent exchange with water (middle), and aerogels after supercritical CO₂ drying (bottom). (c-f) The 3D printed Kevlar cryogel cellular structure with patterns of triangular (c), woodpile (d), honeycomb (e), and wave (f).

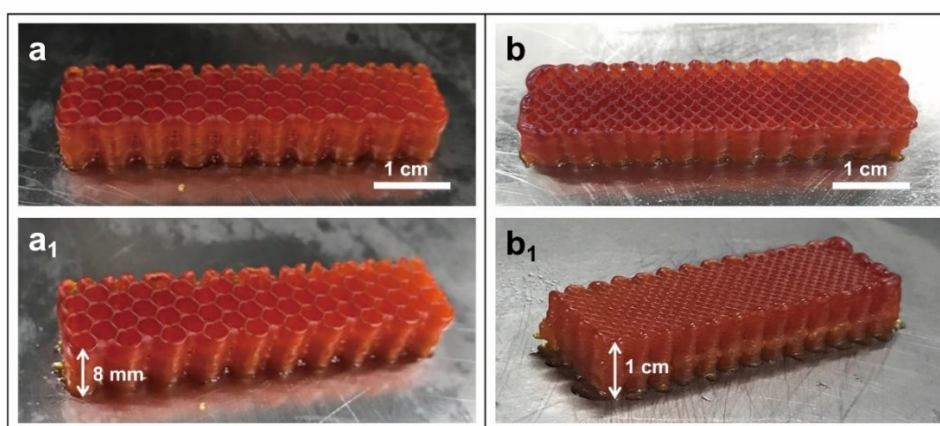


Fig. S11 Digital photos of the 3D printed Kevlar cryogels with a height of 8 mm (a, a₁)

and 1 cm (b , b_1) respectively. Because the 3D cryo-printing method developed in the manuscript was based on a cold plate connected with a thermostatic water bath and the printing process was carried in an open environment, the thickness of the 3D printed architectures is limited. With the increasing height of 3D printing, the worse the freezing crystallization, the worse the printing effect.

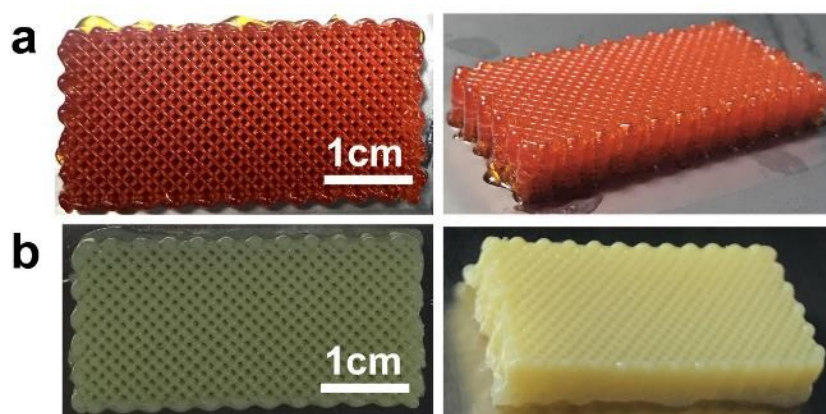


Fig. S12 Digital photos of the 3D printed Kevlar cryogel (a) and hydrogel formed by exchanging with water at the temperature of 4-6 °C (b).

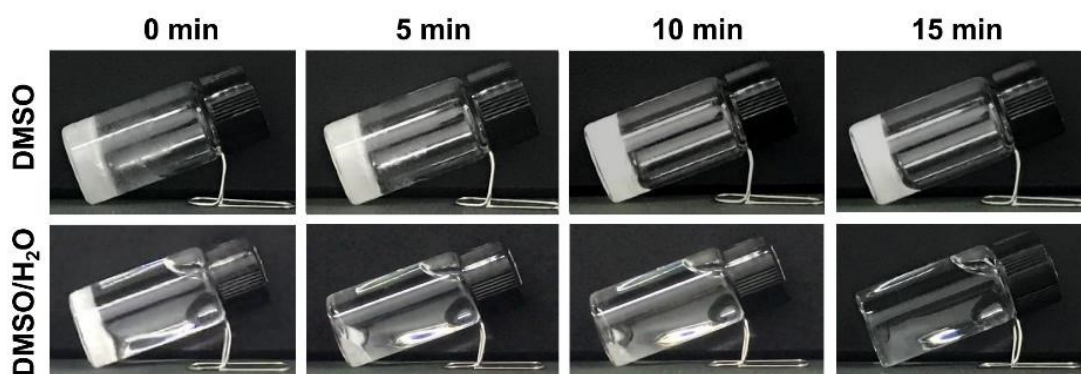


Fig. S13 Digital photos of DMSO and DMSO/H₂O with a volume ratio of DMSO to H₂O of 1:4 at 4 °C. As illustrated, DMSO is in the frozen state at 4 °C and DMSO crystal is gradually dissolved at the solid-liquid interface rather than being molten in

the first place when being mixed with cold water about 4 °C, which demonstrates that exchange of DMSO with cold water can offset the admixture heat.

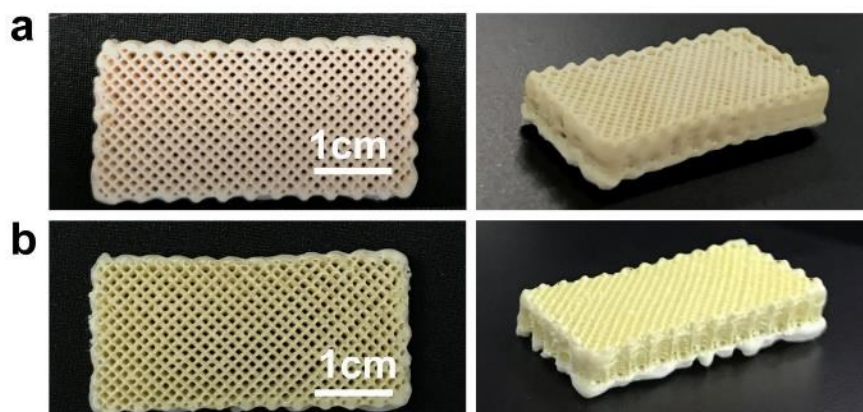


Fig. S14 The digital photos of the 3D printed Kevlar aerogel woodpile by supercritical CO₂ drying (a) and freeze-drying process (b) respectively. The solid structures are able to survive after the freezing drying process, which is similar to the appearance of those after supercritical CO₂ drying

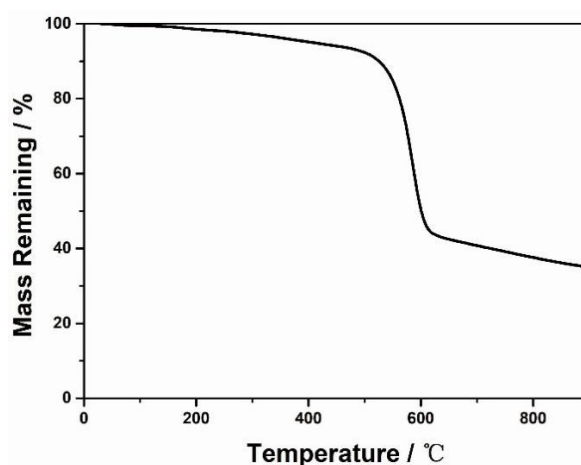


Fig. S15 TGA curve for the 3D-KAAA prepared through freeze-drying process. The weight loss of 6.5% before the degradation of the ANF structure corresponds to the residual water, which demonstrated that the high efficiency of the freeze-drying

process.

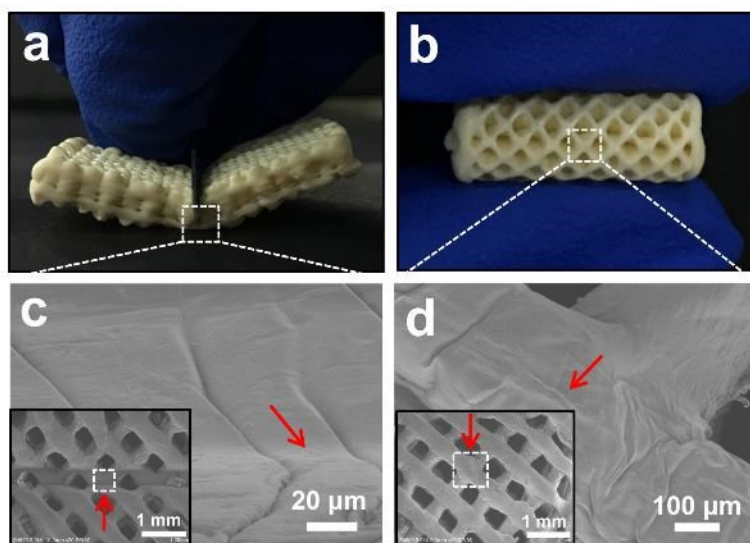


Fig. S16 The digital photos of cutting and bending (a, b) and SEM images of surface of the 3D printed Kevlar aerogel after the external load was removed (c, b). The inset is the corresponding SEM images with a low magnification. The intact morphology after cutting and bending reveal that the 3D printed Kevlar aerogel cellular structure has superior recoverable elasticity.

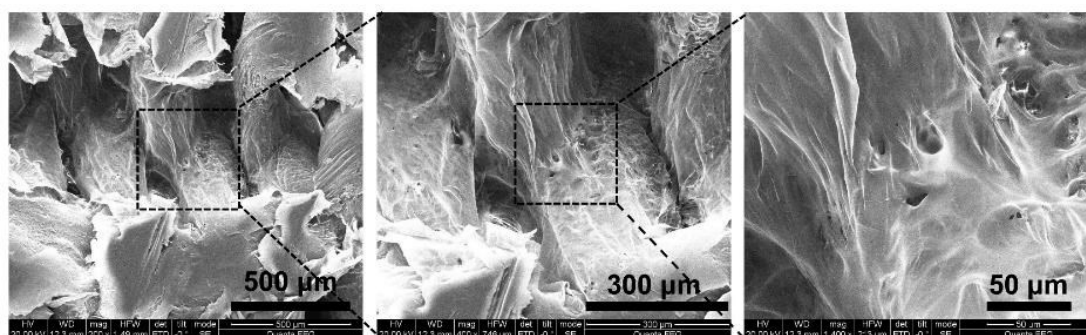


Fig. S17 SEM images of the morphology between the adjacent struts. Interconnection or welding at the junctions between neighboring ANF filament layers is observed.

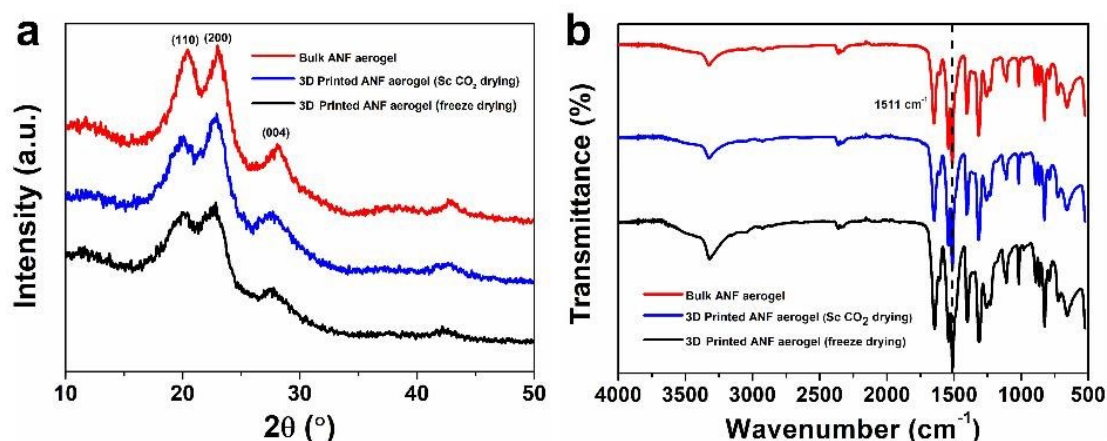


Fig. S18 XRD spectra (a) and FTIR spectra (b) of the raw Kevlar and 3D printed Kevlar aerogel made by either supercritical drying or freeze-drying process. X-ray diffraction (XRD) spectra reveal semicrystalline 3D cellular structure with three diffraction peaks at $2\theta = 20^{\circ}$, 23° and 28° , assigned to the plane of (110), (200), and (004) reflections of monoclinic space group of Kevlar fibre crystals, respectively.⁷ Fourier Transform Infrared (FTIR) Spectra investigate the intensity and sharpness of FTIR peaks (for instance, C-C stretching vibrations of aromatic ring at 1511 cm^{-1}),³ which further proved the negligible change between 3D woodpile after different drying process.

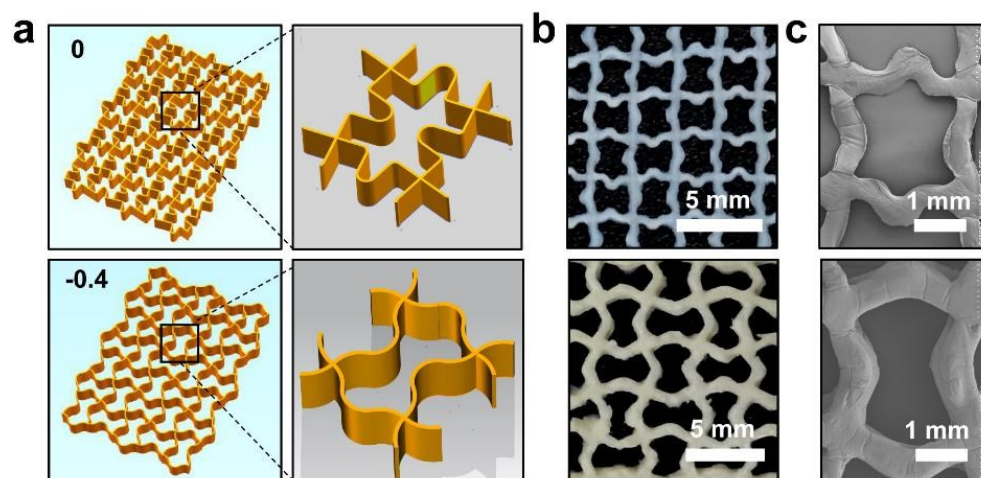


Fig. S19 Designed models of cellular structures with repeated unit cells (a), printed cellular structure (b) and the SEM images of the unit cells (c) of the printed ANF aerogel constructs with different theoretic Poisson's ratio values of 0 and -0.4 .

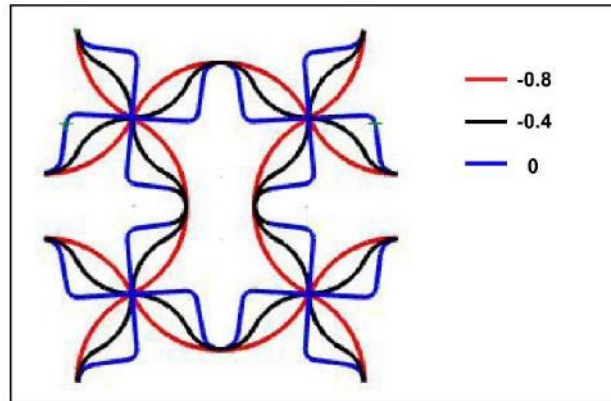


Fig. S20 Schematic diagram of a set of shape-optimized superellipses with theoretical Poisson's ratio values of -0.8 , -0.4 and 0 .

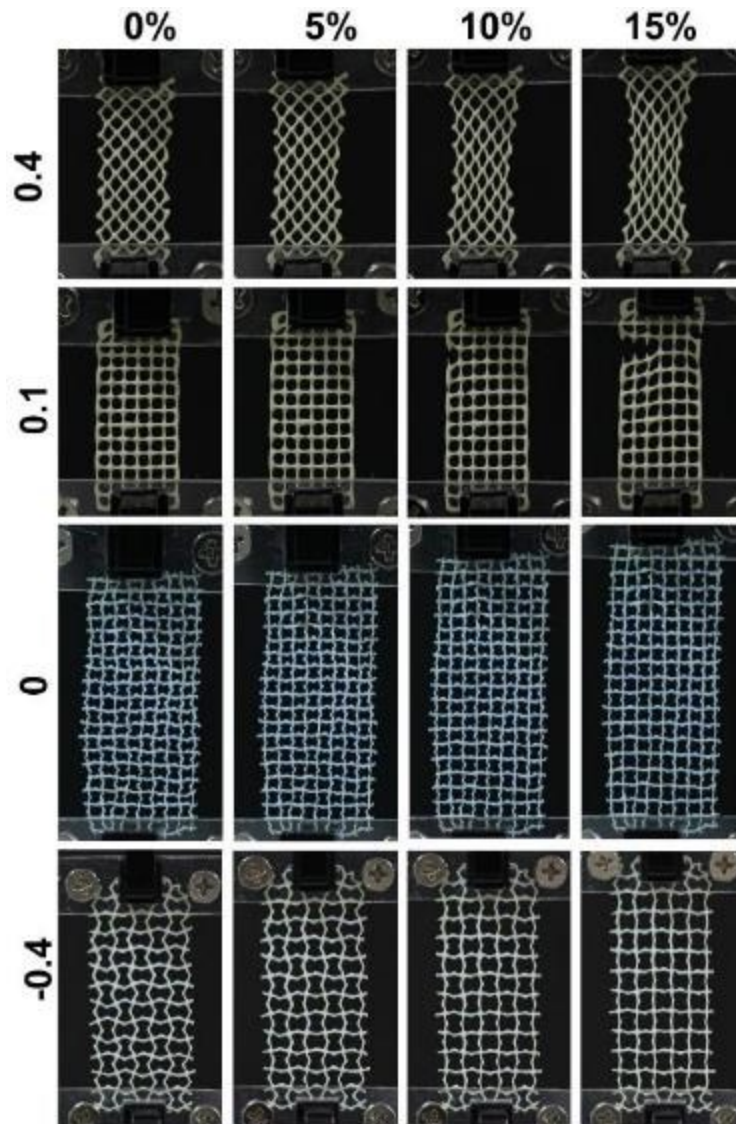


Fig. S21 Deformation of the ANF aerogel structure with different repeated unit cells with a theoretic Poisson's ratio values of 0.4, 0.1, 0, -0.4, under a given longitudinal strain values from 0 % to 15 %.

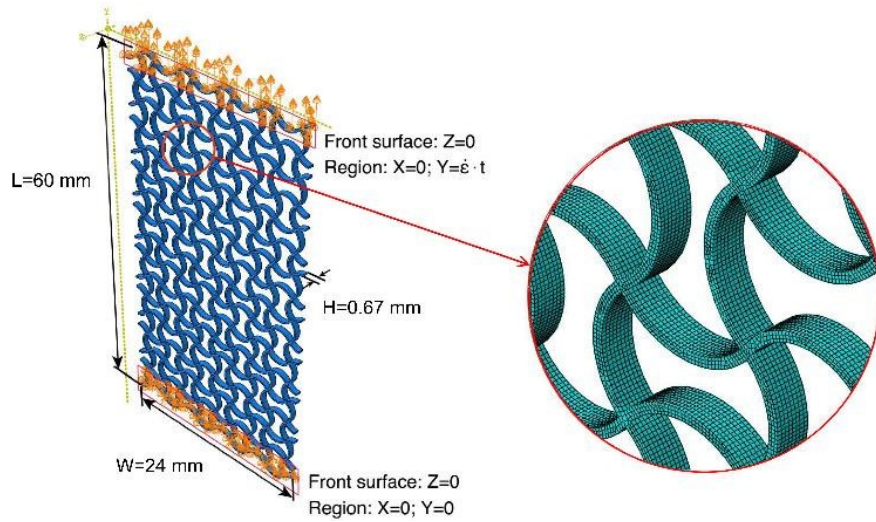


Fig. S22 XFEM modeling of the macroscopic 3D-KAAA. Clamp holders were used to both ends of the specimen with strain applied on the upper end under uniaxial tensile rate of $1 \text{ mm} \cdot \text{min}^{-1}$. Denser meshes are introduced at the joint region.

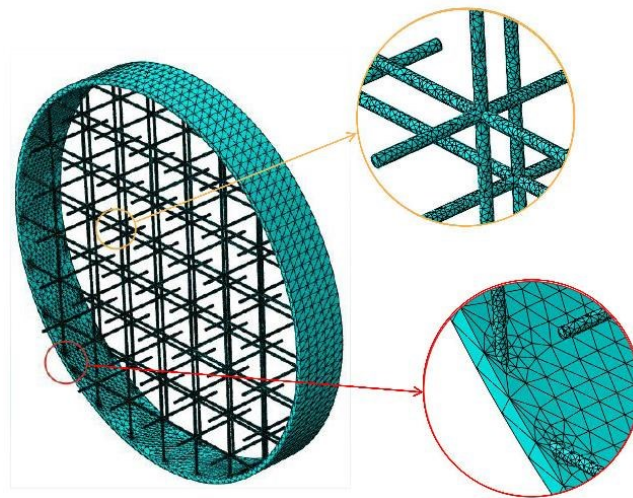


Fig. S23 XFEM modeling of the section of the single strut of 3D-KAAA. The random entangled network of Kevlar nanofibres inside the strut are modelled by using a simplified fully-connected regular beam arrays.

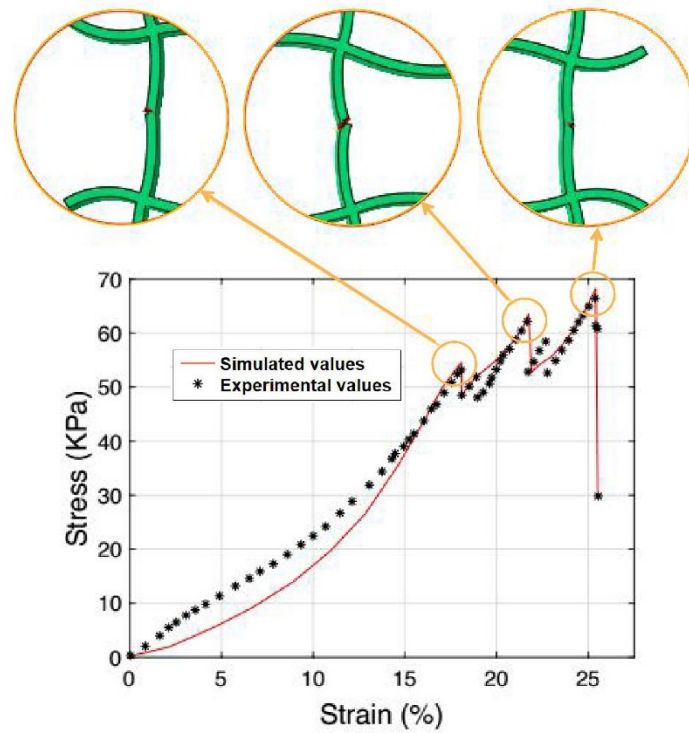


Fig. S24 The simulated stress-strain curve in comparison with the experimental one of the 3D-KAAA with Poisson's ratio of -0.8 and a density of $11.9 \text{ mg}\cdot\text{cm}^{-3}$. A simulated multi-step fracture phenomenon is more or less in agreement with the experimental result shown in Fig. 3f. Each fracture point in the simulation curve can correspond to the experimental one in macroscopic 3D-KAAA in sequence.

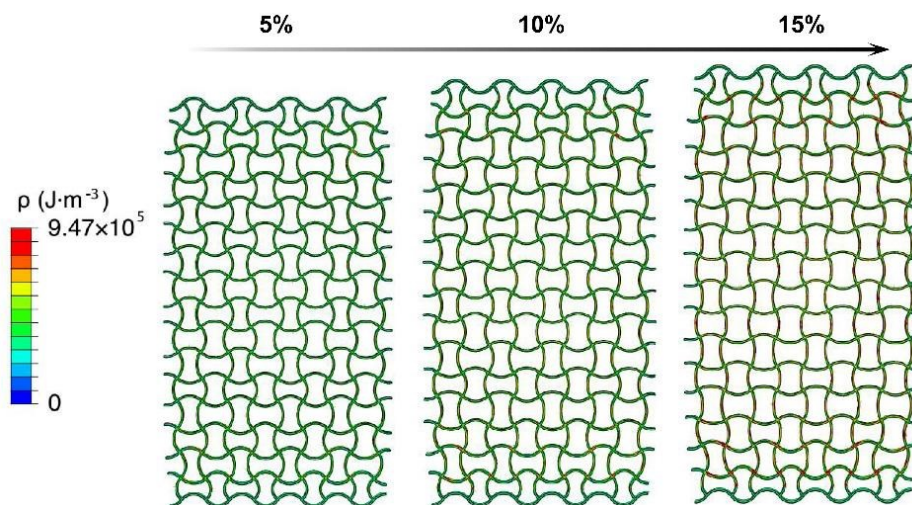


Fig. S25 The tensile energy absorption distribution of the macroscopic 3D-KAAA under different longitudinal strain values of 5 %, 10 % and 15 %. As increasing strain values, the energy absorption is concentrated at the center of the individual struts in 3D-KAAA, which is correlated with strain distribution.

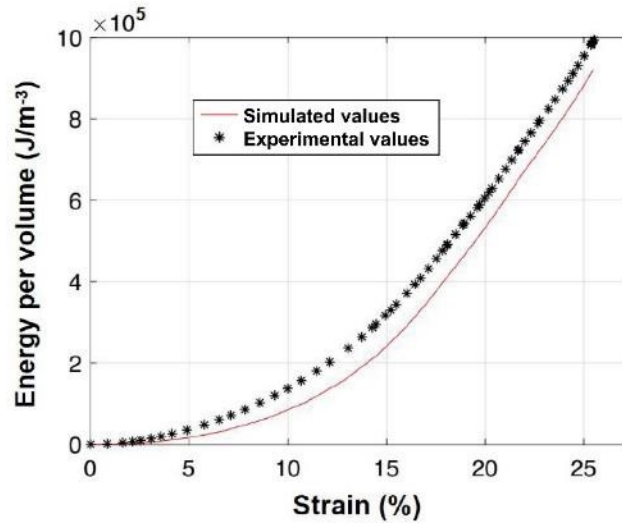


Fig. S26 The simulated plot of the energy per volume as a function of strain of the 3D-KAAA with Poisson's ratio of -0.8 and density of $11.9 \text{ mg}\cdot\text{cm}^{-3}$. The energy per volume increases as the strain is increased. The energy per volume value is $883,000 \text{ J}\cdot\text{m}^{-3}$ at 25 % strain, which is close to the experimental result of $953,000 \text{ J}\cdot\text{m}^{-3}$.

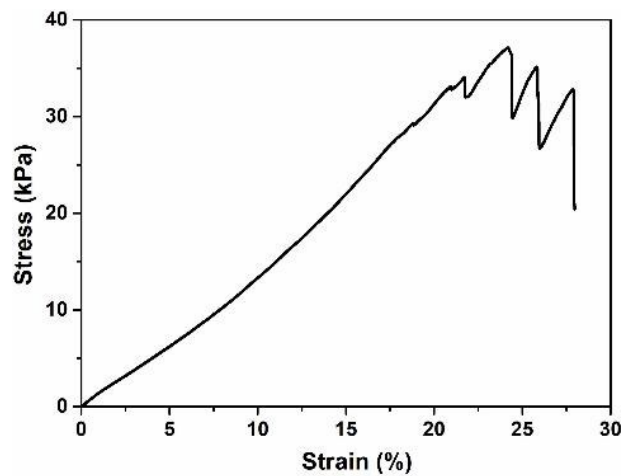


Fig. S27 The tensile stress-strain curve of the 3D printed Kevlar aerogel with Poisson's ratio of 0.4 and a density of $21.0 \text{ mg}\cdot\text{cm}^{-3}$. The energy per volume value is $545,762 \text{ J}\cdot\text{m}^{-3}$ at 25 % strain.

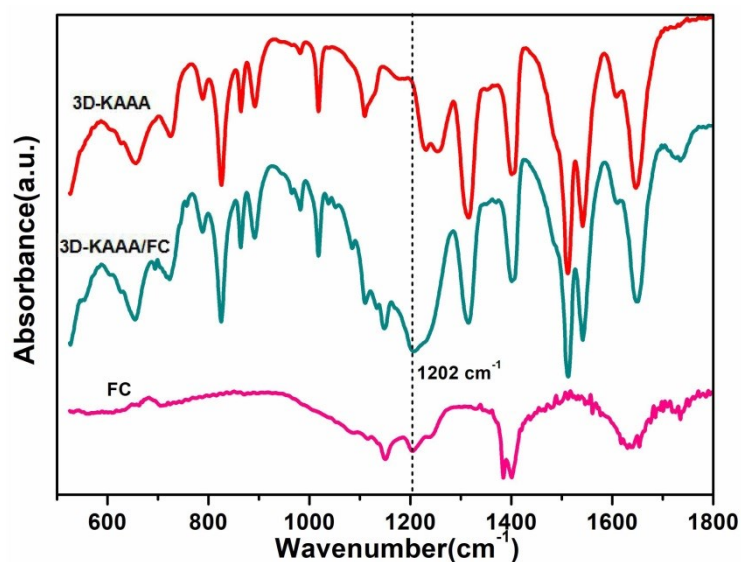


Fig. S28 FTIR spectra of the 3D-KAAA, FC and 3D-KAAA/FC. FTIR spectra reveal that the FC is coated on the surface of 3D-KAAA successfully due to the appearance of the characteristic peak of $-\text{CF}_3$ at 1202 cm^{-1} .

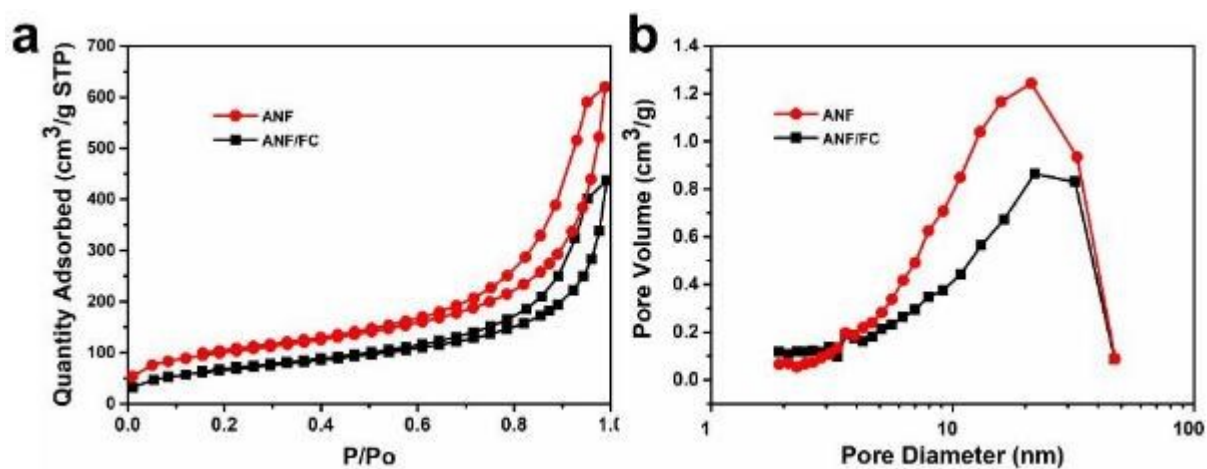


Fig. S29 Nitrogen adsorption-desorption isotherms (a) and pore volume (b) of 3D-

KAAA with and without FC coating. After FC coating, the surface area, S_{BET} , and pore volume is reduced to approximately $238 \text{ m}^2\cdot\text{g}^{-1}$ and $0.676 \text{ cm}^3\cdot\text{g}^{-1}$ from original $350 \text{ m}^2\cdot\text{g}^{-1}$ and $0.959 \text{ cm}^3\cdot\text{g}^{-1}$, respectively.

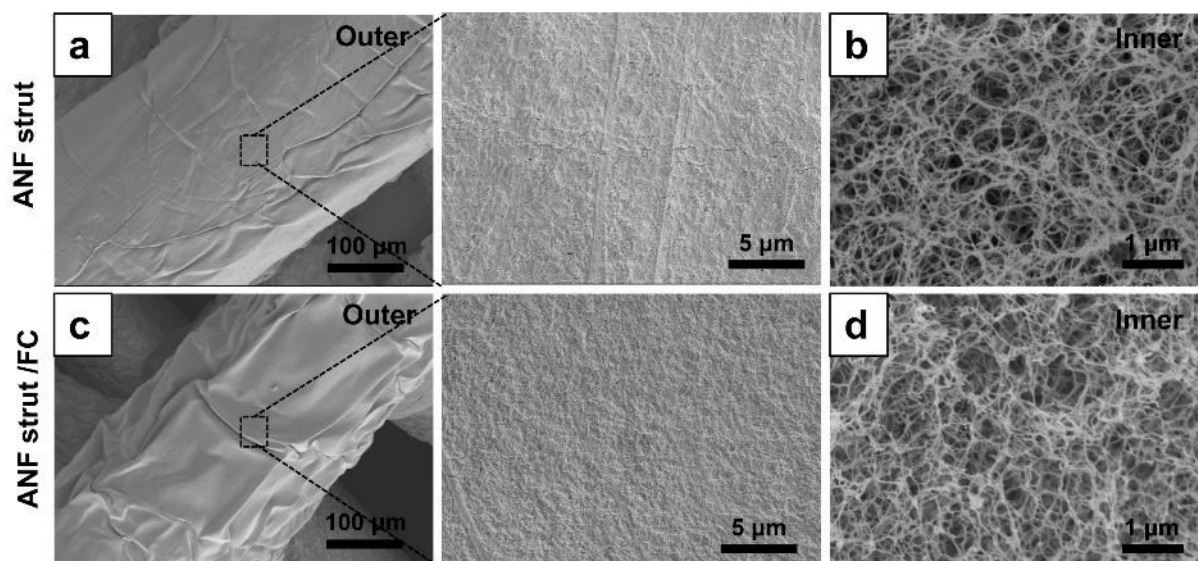


Fig. S30 SEM micrographs of the ANF strut in 3D-KAAA before ((a) for the outer and (b) for the inner) and after FC coating ((c) for the outer and (d) for the inner). The smoother surface of 3D-KAAA is observed after treating with FC.

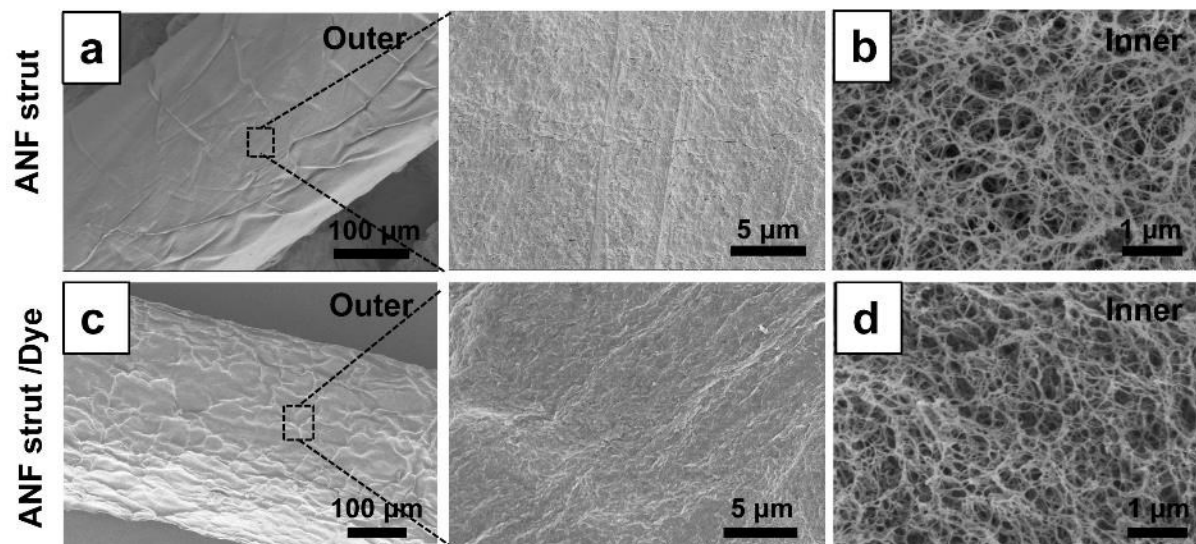


Fig. S31 SEM micrographs of the ANF strut in 3D-KAAA before ((a) for the outer and (b) for the inner) and after dyeing ((c) for the outer and (d) for the inner), demonstrating little change of the microstructure before and after absorbing dyes into 3D architecture.

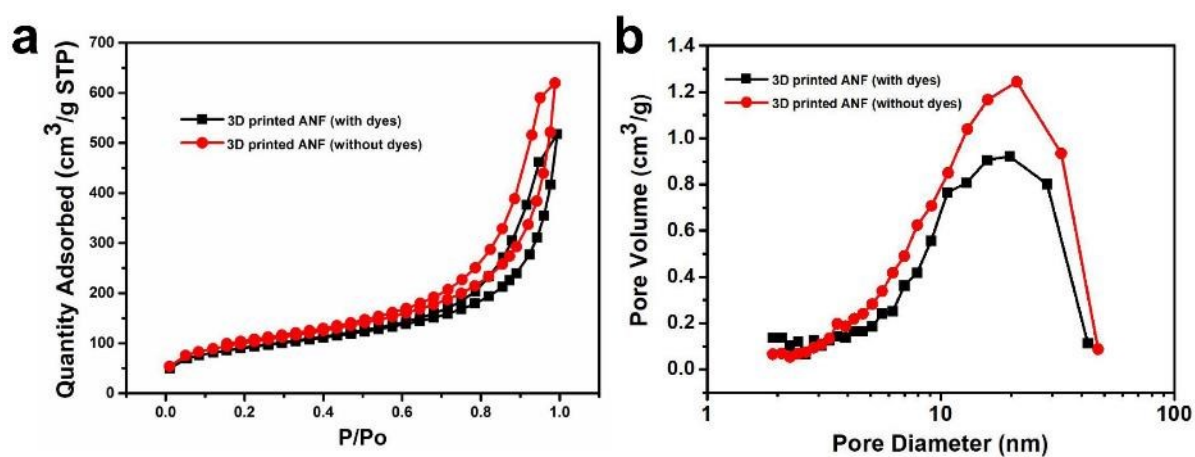


Fig. S32 Nitrogen adsorption-desorption isotherms (a) and pore volume (b) of the 3D-KAAAs with and without dyes, demonstrating little change of the S_{BET} and pore

volume before and after absorbing dyes into 3D architecture.

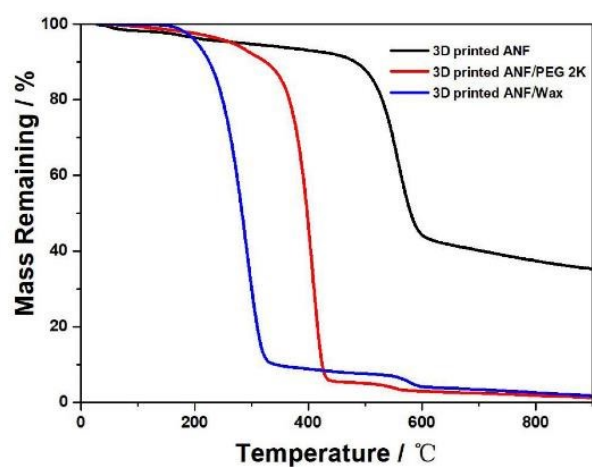


Fig. S33 TGA curves for the 3D-KAAA, 3D-KAAA/PEG-2K and 3D-KAAA/Wax.

The main decomposition process of 3D-KAAA appeared at 518 °C-587 °C, indicating the extraordinary thermal stability of Kevlar aerogel. However, rapid reduction of thermal decomposition temperature of the 3D-KAAA/PEG-2K at 375 °C-425 °C and 3D-KAAA/Wax at 244 °C-317 °C, which is triggered by the decomposition of PEG-2K and Wax at lower temperatures, respectively. From the weight loss, the loading amount of PEG-2K is estimated about 93.5 % and that of the Wax about 91.8 % in the 3D-KAAA/PCM hybrids, respectively.

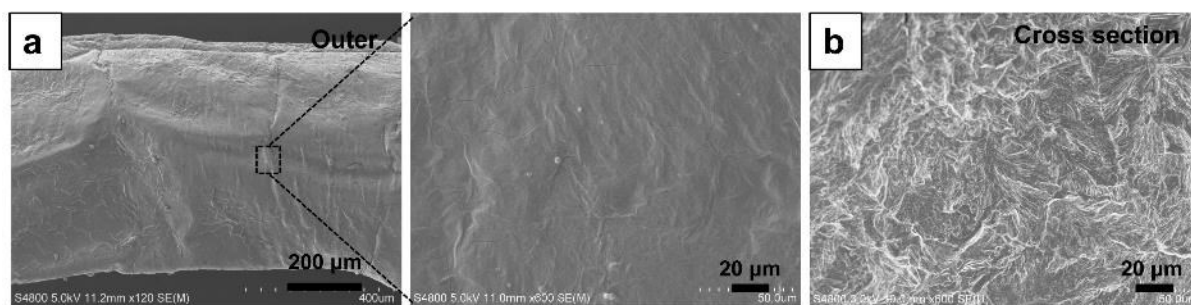


Fig. S34 SEM micrographs of the outer (a) and cross section (b) of the 3D-KAAA/PEG-2K composites, revealing that the PCM is impregnated uniformly throughout the pores within the struts.

Supplementary References

- 1 B. Yang, L. Wang, M. Zhang, J. Luo, Z. Lu and X. Ding, *Adv. Funct. Mater.*, 2020, 2000186.
- 2 B. Yang, M. Zhang, Z. Lu, J. Tan, J. Luo, S. Song, X. Ding, L. Wang, P. Lu and Q. Zhang, *Carbohydr. Polym.*, 2019, **208**, 372-381.
- 3 M. Yang, K. Cao, L. Sui, Y. Qi, J. Zhu, A. Waas, E. M. Arruda, J. Kieffer, M. D. Thouless and N. A. Kotov, *ACS Nano*, 2011, **5**, 6945-6954.
- 4 N. Ogata, K. Sanui and S. Kitayama, *J. Polym. Sci., Part A: Polym. Chem.*, 1984, **22**, 865-867.
- 5 H. J. Kong, X. M. Ding, M. M. Qiao, Y. Wu and M. H. Yu, *Iop Conf.*, 2017, **213**, 012044.
- 6 J. Zhu, M. Yang, A. Emre, J. H. Bahng, L. Xu, J. Yeom, B. Yeom, Y. Kim, K. Johnson and P. Green, *Angew. Chem. Int. Ed.*, 2017, **56**, 11744-11748.

7 J. Zhu, W. Cao, M. Yue, Y. Hou, J. Han and M. Yang, *ACS Nano*, 2015, **9**, 2489-2501.